Available online at www.sciencedirect.com

SciVerse ScienceDirect

Ceramics International 39 (2013) 6207–6213

CERAMICS INTERNATIONAL

www.elsevier.com/locate/ceramint

Laser surface modification of alumina: Integrated computational and experimental analysis

Marco A. Moncayo, Soundarapandian Santhanakrishnan, Hitesh D. Vora, Sameer R. Paital, Narendra B. Dahotre*

Department of Materials Science and Engineering, Laboratory for Laser Materials Processing & Synthesis, University of North Texas, 1155 Union Circle # 305310, Denton, TX 76203-5017, USA

Received 9 January 2013; accepted 14 January 2013
Available online 1 February 2013

Abstract

In this work, both computational heat transfer model and experimental investigations were used for understanding the evolution of microstructures of the laser processed alumina with a single laser track, subjected to various processing conditions ($64–128 \times 10^6$ J/m^2). The influence of laser energy density on the change of surface temperature and cooling rate of laser processed alumina samples were extracted. Furthermore, the modeling results were correlated to determine the variation on the surface topography, grain size, and porosity formation. The results indicated that, by controlling the laser energy density, more multi-faceted grains were formed with less porosity.

Keywords: Laser surface modification; Alumina; Heat transfer modeling; Multi-faceted grains

1. Introduction

Alumina (Al_2O_3) is a commonly used material suitable for various applications such as high temperature and corrosion environments, biomedical, structural, and surface finishing [1–7]. Al_2O_3 possesses some significant mechanical characteristics including high hardness and high wear resistance at elevated temperatures. Alumina is synthesized with varying porosity values. Tools made of alumina material such as a grinding wheel consist of abrasive grains held in place by a low-melting point bond material and has a porosity value ranging from 30 to 40% [8]. As the tool progresses through its life, the abrasive edges on the surface begin to dull and fracture off. As these abrasive edges begin to "dull" or fracture off all together, the surface quality of the work piece and the material removal efficiency of the tool will deteriorate. Furthermore, as the tool begins to remove chips from the work piece, these chips could become embedded in the porous surface of the tool, degrading its material removal efficiency [8].

In order to improve the abrasive characteristics of the tool, new abrasive edges need to be revealed, as well as removal of foreign contaminates embedded in the tool's surface. For this to be done, the tool must undergo surface modification. Surface modification is an operation or process to generate a specific surface topography [8]. The conventional surface modification technique using a dresser embedded with diamond particles to mechanically dress the surface of the tool, revealing "sharp" abrasive features [8,9]. However, this process results in excessive deterioration and loss of tool material. In addition, it also requires to upkeep and replace the diamond dresser in order to maintain for getting adequate consistent results. Laser surface modification (LSM) is a well-established technique for tailoring and improving the surface properties of the tool [8–15]. Furthermore, the high power lasers can ablate any foreign contaminates embedded in the surface of the tool [9]. The objective of this study is to understand the significant effects and fundamentals of LSM of alumina using a single

*Corresponding author. Tel.: +1 940 565 2031; fax: +1 940 565 4824.
E-mail address: Narendra.Dahotre@unt.edu (N.B. Dahotre).

0272-8842/$ - see front matter © 2013 Elsevier Ltd and Techna Group S.r.l. All rights reserved.
http://dx.doi.org/10.1016/j.ceramint.2013.01.040

laser track for various processing conditions in order to improve its microabrasive qualities.

2. Experimental procedures

Commercially available alumina (82% Al_2O_3 and balance of ceramic/glass bonding material, purchased from Colonial West Abrasives, CA) at a size of $50 \times 50 \times 30$ mm^3 was used in this study for LSM. An ytterbium doped Nd-YAG laser system (IPG—YLS 3000), equipped with a fiber-optic beam delivery system was used in a continuous mode for processing the alumina sample (Fig. 1). A single laser track was used on each alumina sample for various laser processing conditions (Table 1).

The laser energy density (LED) was calculated using the following equation:

$$\text{Laser energy density} = \frac{2P}{\pi r v} \quad (1)$$

where P is the laser power (W), r is the beam radius (mm), and v is the scanning speed (m/s) [16]. A FEI Quanta 200 environmental scanning electron microscope (ESEM) system in a high vacuum chamber with a low accelerating voltage ($\sim$5 kV) was used to obtain the microstructural features of the laser processed alumina samples. ImageJ was used to reveal and statistically determine the grain size and percentage of porosity remaining in the laser modified alumina.

3. Computational modeling

Using a COMSOL Multiphysics®, a two-dimensional (2-D) heat transfer model was constructed (Fig. 2). The model was used to predict the change in temperature and cooling rates for various laser processing conditions. For simplicity, a continuous mode laser beam with a symmetrical Gaussian shape energy distribution was incorporated into the 2-D model. This approach was used to represent any location that has undergone to the laser interaction during the residence time (t_r, s). By using the laser beam diameter (D, m) and laser scanning speed (v, m/s), the residence time ($t_r = D/v$) can be determined. A porosity value of 40% was selected for the model.

The phase change of the material was incorporated to accurately obtain the data from calculations. When the material has undergone this phase change, a significant amount of latent heat was released. This has a considerable effect on the specific heat, C_p, of the alumina. To compensate the latent heat of the phase change, the value of C_p was changed to C_p1 [17].

$$C_p1 = C_p + \delta\Delta H + \left(\frac{\Delta H}{T_m}\right) Z((T - T_m), \Delta T) \quad (2)$$

$$\delta = \frac{\exp\left(-(T - T_m)^2/(\Delta T)^2\right)}{\Delta T\sqrt{\pi}} \quad (3)$$

where δ is a Gaussian curve, ΔH is the latent heat of change, and T, T_m are instantaneous and melting temperatures, respectively. ΔT represents the phase transition temperature range, and Z is the smooth Heaviside function [17]. For this model, constant values of the thermal conductivity and density were considered (Table 2).

For simplicity, the dimensions of the model were set to 5 mm length and 3 mm width. These dimensions were chosen specifically to accurately observe the heat transfer physics that

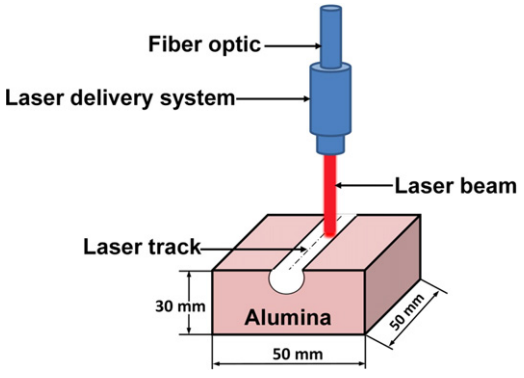

Fig. 1. Schematic of laser surface modification of an alumina sample.

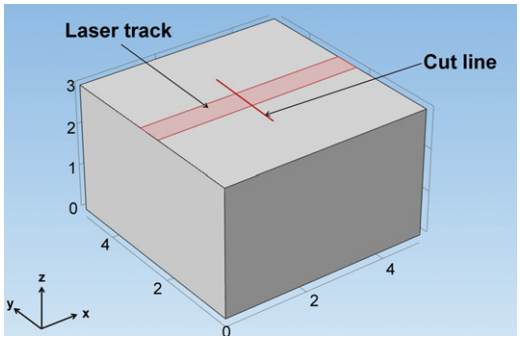

Fig. 2. COMSOL image showing the edge and boundary domains as well as the cut plane.

Table 1
Laser processing parameters.

Laser power (W)	Scanning speed (m/s)	Beam diameter (m)	Laser energy density (10^6 J/m^2)
600	0.020	0.6×10^{-3}	64
800	0.020	0.6×10^{-3}	85
1000	0.020	0.6×10^{-3}	107
1200	0.020	0.6×10^{-3}	128

occurred during the laser processing on the samples. The model used a moving laser beam with a beam diameter of 0.6×10^{-3} m that was traveling across the surface of the sample. Boundary domains and edge domains were used in the model to measure the temperature changes within the sample. The boundary domain measured the change in temperature at the center of the laser track while the edge domains measured the change in temperature along the sides of the laser track. A "cut line" containing multiple virtual probes was also used to measure the temperatures across the width of the laser track (Fig. 3a). A similar cut line was used along the z-axis, starting from the top ($z=3.0$ mm) and ending at $z=1.5$ mm for the interval of 0.01 mm (Fig. 3b).

Table 2
Material properties of alumina [18].

Property	Symbol	Value
Absorptivity	A	0.25
Thermal conductivity	k	35 W/(mK)
Density	ρ	3.8 g/cm^3
Latent heat of melting	ΔH	1067.43 J/g
Latent heat of vaporization	L_v	1066.5 J/g
Melting temperature	T_m	2324 K
Vaporization temperature	T_v	3273 K
Half-width of the temperature curve	ΔT	30 K

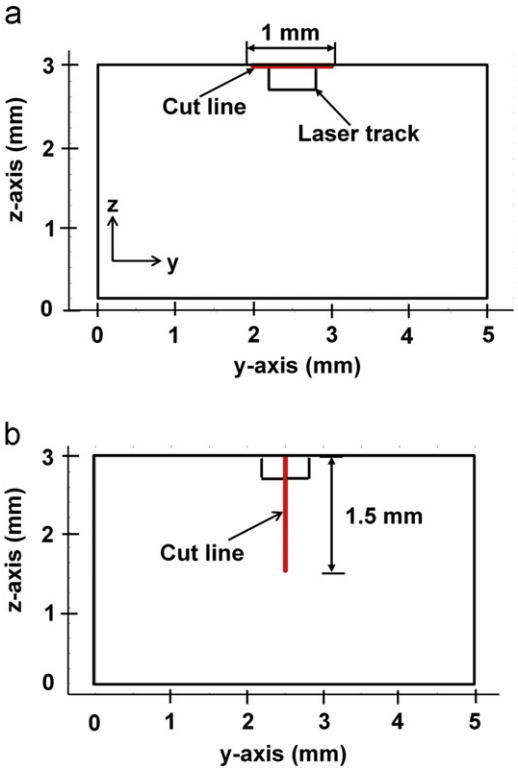

Fig. 3. Location of cut planes in (a) y and (b) z directions for two-dimensional model.

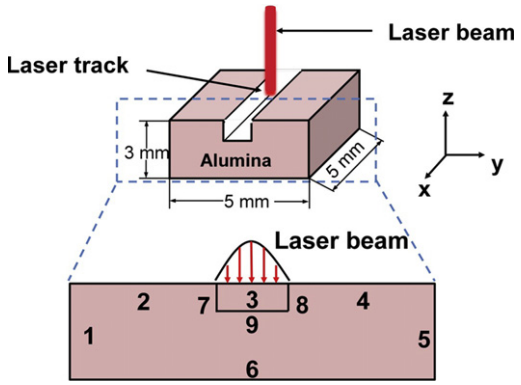

Fig. 4. Locations for boundary conditions of the computational model.

3.1. Meshing

Two types of meshing such as an extremely fine and normal mesh conditions were used for the edge domain boundaries and the remaining regions. The maximum and minimum sizes for extremely fine mesh are 0.0201 mm and 6×10^{-4} mm, respectively. The normal mesh elements maximum and minimum sizes are 0.105 mm and 0.03 mm, respectively.

3.2. Governing equations and boundary conditions

The equation (Eq. (4)) that governs the heat transfer for this model is described as below:

$$\frac{\partial}{\partial y}\left(k\frac{\partial T}{\partial y}\right)+\frac{\partial}{\partial z}\left(k\frac{\partial T}{\partial z}\right)+q'' = \rho c_p \frac{\partial T}{\partial t} \tag{4}$$

where q'' is the heat flux (W/m^2), ρ is the density of the material (kg/m^3), c_p is the specific heat per unit mass (J/kg K), and k is the thermal conductivity of the material (W/m K). The boundary conditions used in the computational model are illustrated in Fig. 4 and defined in Table 3. Boundary 3 underwent exposure to the laser beam, convective cooling, and surface-to-ambient radiation simultaneously (Eq. (5)).

$$-k\frac{\partial T}{\partial z} = \beta A P_g - h[T-T_0] - \varepsilon\sigma\left[T^4-T_0^4\right] \tag{5}$$

where β represents the active state of the laser beam ($\beta=1$ for $0 \le t \le t_r$ and $\beta=0$ for $t > t_r$), h is the convective heat transfer coefficient ($h=10$ W/m^2 K), ε is the emissivity of alumina ($\varepsilon=0.7$) for thermal radiation, and σ is the Stefan–Boltzmann constant ($\sigma=5.67 \times 10^{-8}$ W/m^2 K^4) [18].

The Gaussian power distribution for a moving laser beam is governed by the following equation:

$$P_g = A\left[\frac{P}{(\pi/4D^2)}\right]\exp\left[-\left(\frac{(x-\mathrm{loc}x)}{2\emptyset^2}\right)\right] \tag{6}$$

where P_g is laser power density (W/m^2), loc$x$ is the location along the x-axis, P is the laser power (W), and $\emptyset$ is the standard deviation of P_g. Boundaries 1–5 undergo surface-to-ambient and convection cooling conditions. Boundaries 2–4 followed Eq. (7) while boundaries 1 and 5 followed

Table 3
Boundary conditions.

Description	Boundary no.	Boundary condition	Variable
Laser beam	3	Heat flux	P_g
Radiation	1–5	Surface-to-ambient	ε
Natural convection cooling	1–5	Convective cooling	h
Insulation	6	Insulation	–

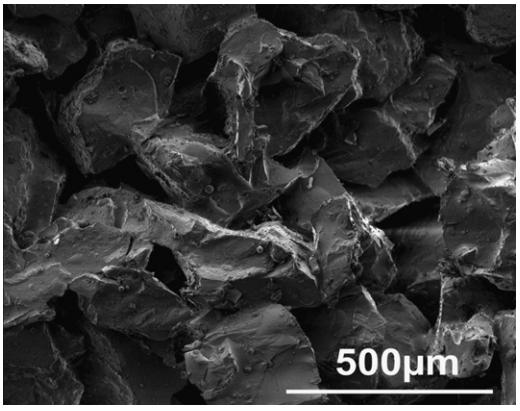

Fig. 5. SEM image of the unprocessed surface of the alumina.

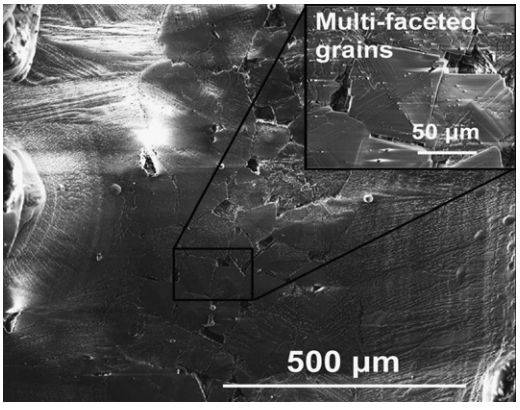

Fig. 6. SEM image of the laser surface modified alumina sample at 64×10^6 J/m^2.

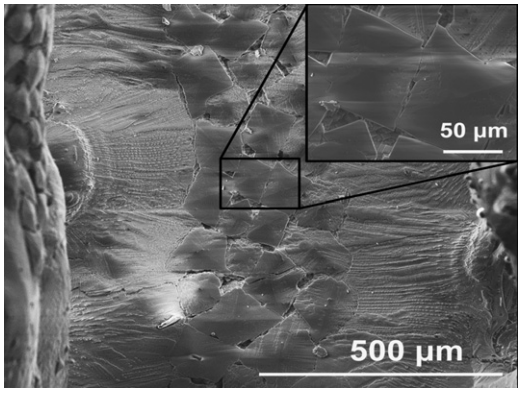

Fig. 7. SEM image of the laser surface modified alumina sample at 85×10^6 J/m^2.

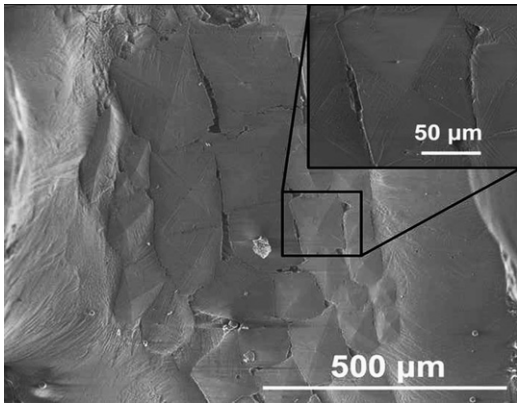

Fig. 8. SEM image of the laser surface modified alumina sample at 107×10^6 J/m^2.

Eq. (8). Boundary 6 was considered to be an insulated boundary followed Eq. (9).

$$-k\frac{\partial T}{\partial z} = h[T-T_0]-\varepsilon\sigma\left[T^4-T_0^4\right] \quad (7)$$

$$-k\frac{\partial T}{\partial y} = h[T-T_0]-\varepsilon\sigma\left[T^4-T_0^4\right] \quad (8)$$

$$-k\frac{\partial T}{\partial y} = 0 \quad (9)$$

4. Results and discussion

Using COMSOL Multiphysics®, the change in temperature and cooling rate of laser modified alumina samples for various laser processing conditions ($64–128 \times 10^6$ J/m^2) were predicted. The temperature profile (Fig. 5) across the width of the laser track was obtained for each laser processed alumina sample. The center of the laser track is located at 0 m on the y-axis. The total width of the laser track is 0.6×10^{-3} m. The predicted temperature for all the laser processed samples along the laser track has indicated that the temperature exceeded the melting (T_m) and vaporization temperatures (T_v). As the LED increased, the temperature also increased. The temperature profile for each laser processed sample resembled the Gaussian distribution that generated a non-uniform temperature profile across the laser track. At LED of 64×10^6 J/m^2, the temperature of the laser processed sample was above the melting temperature but a small region experienced vaporization temperature. The laser processed sample at 128×10^6 J/m^2

showed that the entire laser track has undergone for melting as well as vaporization.

For each processing condition, the temperature readings taken at the center of the track were different, significantly from those obtained at the center of the laser track (Fig. 6) At the center of the laser track, all of the samples exhibited above melting and vaporization temperatures (Fig. 6b). In contrary, at the edge of the laser track, the samples processed at 107×10^6 J/m^2 and 128×10^6 J/m^2 only were exhibited above melting and vaporization temperatures (Fig. 6c), respectively. It can be noted that, as the LED increases, more heat was penetrating toward the depth (z-axis) of surface, resulting in the increase of temperature (Fig. 7). It is important to note that as the LED increases, a larger portion of each respective sample experiences readings above the melting temperature (T_m) and vaporization temperature (T_v). The melt and vaporization depths increased steadily as the LED increased (Fig. 8). Subsequently, the material removal due to vaporization increased as the LED increased (Fig. 9). Similarly, the area of melting and vaporization increased as the LED increased. It is necessary to control the amount of vaporization as much as possible in order to avoid the material loss and retain the base material properties.

A non-uniform cooling rate was obtained across the laser track as the result of using the Gaussian energy distribution. It was evidently seen that higher cooling rates

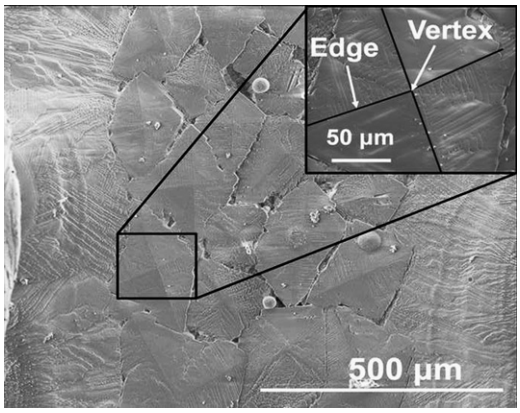

Fig. 9. SEM image of the laser surface modified alumina sample at 128×10^6 J/m^2.

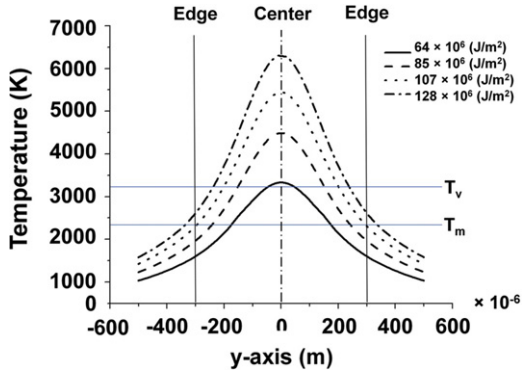

Fig. 10. Change in temperature along the width of the laser track.

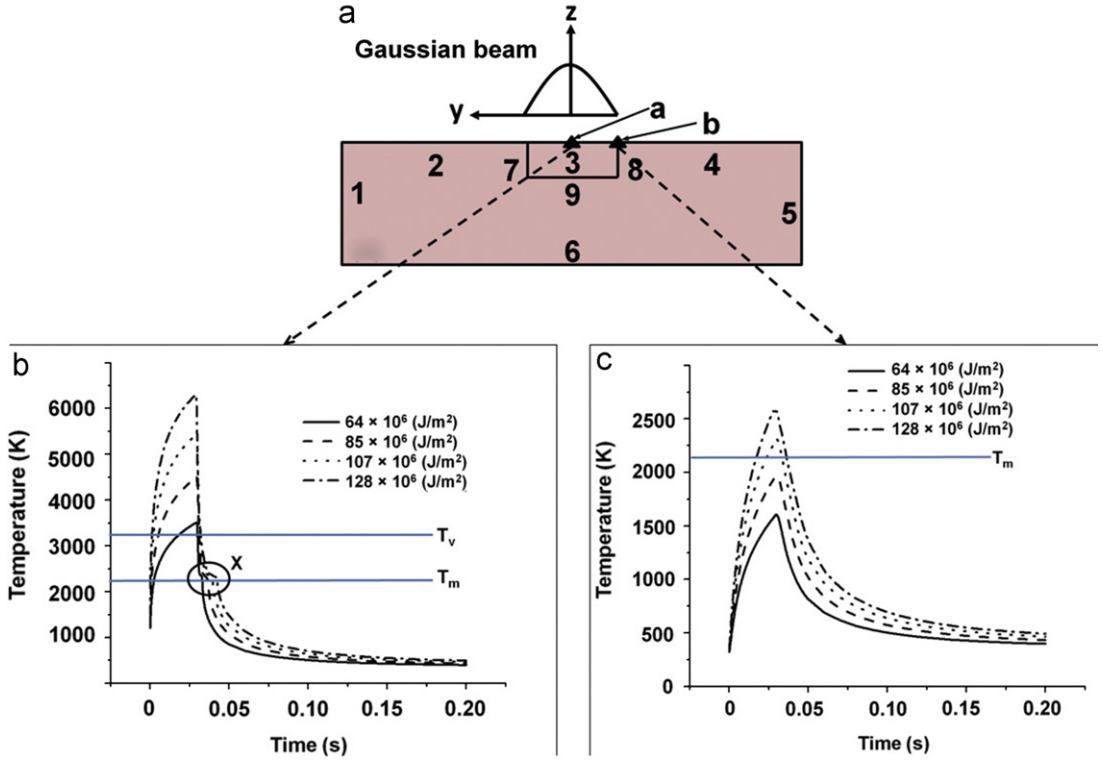

Fig. 11. A schematic of (a) the two-dimensional COMSOL model (b) temperature along the center and (c) temperature along the edge. Note: Point X depicts a rise in temperature due to the latent heat released during the phase change from liquid to solid.

were obtained at the center of laser track and further it decreased while moving toward the edge (Fig. 10). It was reported that the laser modified surface topography was the function of the LED, temperature history and cooling rate [11,15]. Therefore, analyzing the samples' surface topography, correlation with the modeling results could extract more understanding in this study.

As previously mentioned, alumina is generally a porous material, consisting of sintered alumina grains (Fig. 11). The sharp abrasive edges of alumina particles inhabited the continuous porous surface of the alumina. The grain boundaries were not clearly defined, but the edges of the particles were visible. The physical topographical feature (multi-faceted grains) contributes the enhanced abrasive qualities of the LSM alumina. After LSM, these grains were noticeable along the surface of the alumina sample (Figs. 12–15).

Within the center of the laser tracks, multi-faceted grains were represented as the main microstructure feature (Figs. 12–15). Columnar primary dendrites are formed along the boundary of the grain region, extending to the edges of the track. However, each processed sample has displayed different topographical characteristics at the center of the laser track. At higher LED (107 and 128×10^6 J/m^2), very clear multi-faceted grains were observed in the laser modified samples (Figs. 14,15). It can be noticed that, at these higher LED only, they have generated higher temperatures above vaporization (Fig. 5) and higher cooling rates (Fig. 10). Even at lower LED (64 and 85×10^6 J/m^2) also, the multi-faceted grains were seen but with less distinctive features (Figs. 12,13). The reason could be that at lower LED (64 and 85×10^6 J/m^2), the samples did not experience the higher temperature and cooling rates.

Multi-faceted grains with large diameters were produced in the center of the laser tracks. Most of the grains were formed in to symmetrical "parallelogram like" shapes (Figs. 12–15). A well-formed grain has four faces, four edges and one vertex where the edges meet (Fig. 15b). After LSM, the porosity of the alumina's surface decreased substantially. The LED greatly influenced the formation of porosity (Table 4). The samples that were processed with LED of 107 and 128×10^6 J/m^2, have shown much larger grains. For these higher LED values, well defined abrasive edges were obtained (Figs. 14,15). These edges play a major role to improve the abrasive characteristics. This is a good indication that these laser processing parameters can produce the desired change in the microstructure of the alumina sample.

Using the image-processing program (Image J), the average diameter of the multi-faceted grains for each respective

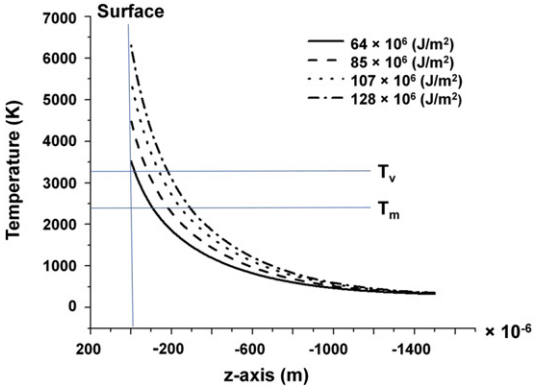

Fig. 12. Change in temperature profile at the center of the laser track.

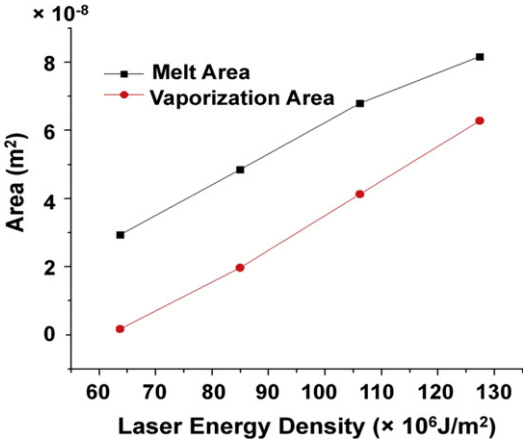

Fig. 14. Melting and vaporization areas as a function of laser energy density.

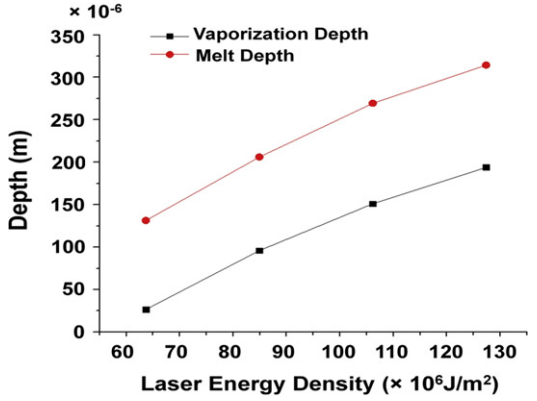

Fig. 13. Melting and vaporization depths as a function of laser energy density.

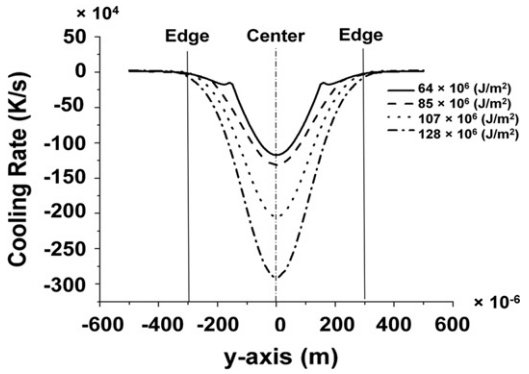

Fig. 15. The cooling rates for various laser processing parameters along the width of the laser track.

Table 4
Average diameter of multi-faceted grains and porosity percentage for each sample.

Laser energy density (10^6 J/m^2)	Average diameter (μm)	Porosity (%)
64	166.55 ± 2.05	2.36
85	168.94 ± 1.61	1.19
107	226.98 ± 1.95	1.13
128	225.83 ± 1.91	0.84

sample was measured. The porosity percentages of the laser processed samples were also obtained (Table 4).

As the LED increased, the average diameter of the fine multi-faceted grains increased. In addition, the surface porosity of the laser affected region has also substantially reduced. For this study, a constant laser surface modified area (0.9871 mm^2) was chosen for the calculation of grain size and porosity percentage for each laser processed sample. From the SEM analysis, the samples that underwent the LED of 107 and 128×10^6 J/m^2 or more demonstrated a denser and more closely grouped multi-faceted grain formation. The porosity within the laser processed alumina's surface exhibited a decreasing trend as the LED increases. This is exceptionally important in order to provide more abrasive edges along the surface in the form of multi-faceted grains. It can be concluded that as the LED increased, the surface temperature and cooling rate increased which in turn directly influenced the formation of larger size of multi-faceted grains with less porosity.

5. Conclusions

As the laser energy density increased ($64 \rightarrow 128 \times 10^6$ J/m^2), the cooling rate increased ($1.1 \rightarrow 2.9 \times 10^4$ K/s), that subsequently increased the grain size (70 → 160 μm) and decreased the porosity (2.4 → 0.8%). This provided substantial evidence and supported the claim that the controlled laser energy density ($107–128 \times 10^6$ J/m^2) has generated well-defined multi-faceted grains (225 μm) with less porosity (1%). The results of this study have envisaged to pursuit of multiple laser track work of alumina.

Acknowledgment

The authors would like to acknowledge the financial support from the National Science Foundation (NSF-CMMI 1010494).

References

[1] S.N. Paglieri, K.Y. Foo, J.D. Way, J.P. Collins, D.L. Harper-Nixon, A new preparation technique for Pd/alumina membranes with enhanced high-temperature stability, Industrial and Engineering Chemistry Research 38 (5) (1999) 1925–1936.
[2] Y.-S. Lin, A.J. Burggraaf, Preparation and characterization of high-temperature thermally stable alumina composite membrane, Journal of the American Ceramic Society 71 (1) (1991) 219–224.
[3] M. Herrmann, B. Seipel, J. Schilm, K. Nickel, G. Michael, A. Krell, Hydrothermal corrosion of zirconia-toughened alumina (ZTA) at 200 °C, Journal of the European Ceramic Society 25 (10) (2005) 1805–1812.
[4] S. Deville, Low-temperature ageing of zirconia-toughened alumina ceramics and its implication in biomedical implants, Journal of the European Ceramic Society 23 (15) (2003) 2975–2982.
[5] Y. Josset, Z. Oum'Hamed, A. Zarrinpour, M. Lorenzato, J.J. Adnet, D. Laurent-Maquin, In vitro reactions of human osteoblasts in culture with zirconia and alumina ceramics, Journal of Biomedical Materials Research 47 (4) (1999) 481–493.
[6] Medvedovski Eugene, Alumina-mullite ceramics for structural applications, Ceramics International 32 (4) (2006) 369–375.
[7] M.J. Jackson, B. Mills, Materials selection applied to vitrified alumina and CBN grinding wheels, Journal of Materials Processing Technology 108 (1) (2000) 114–124.
[8] M.J. Jackson, A. Khangar, X. Chen, G.M. Robinson, V.C. Venkatesh, N.B. Dahotre, Laser cleaning and dressing of vitrified grinding wheels, Journal of Material Processing Technology 185 (1–3) (2007) 17–23.
[9] A. Khangar, N.B. Dahotre, M.J. Jackson, G.M. Robinson, Laser dressing of alumina grinding wheels, Journal of Materials Engineering and Performance 15 (2) (2006) 178–181.
[10] S.P. Harmikar, N.B. Dahotre, Evolution of surface morphology in laser-dressed alumina grinding wheel material, Internation Journal of Applied Ceramic Technology 3 (5) (2006) 375–381.
[11] A.A. Khangar, E.A. Kenik, N.B. Dahotre, Microstructure and microtexture in laser-dressed alumina grinding wheel material, Ceramics International 31 (4) (2005) 621–629.
[12] S. Harimkar, N.B. Dahotre, Laser assisted densification of surface porosity in structural alumina ceramic, Physica Status Solidi A 204 (4) (2007) 1105–1113.
[13] S.P. Harimkar, N.B. Dahotre, Rapid surface microstructuring of porous alumina ceramic using continuous wave Nd:YAG laser, Journal of Materials Processing Technology 209 (10) (2008) 4744–4749.
[14] A. Samant, S. Paital, N. Dahotre, Process optimization in laser surface structuring of alumina, Journal of Materials Processing Technology 203 (1–3) (2008) 498–504.
[15] S.P. Harimkar, N.B. Dahotre, Effect of laser fluence on surface microstructure of alumina ceramic, Advances in Applied Ceramics 105 (6) (2006) 304–308.
[16] Energy Density of a Laser Beam, CORE-Materials, University of Liverpool. Available from: 〈http://core.materials.ac.uk/search/detail.php?id=3213〉 (accessed 14.09.10).
[17] J. Fjellsted, Continuous Casting, Model Documentation, COMSOL Multiphysics, 2011. Available from: 〈http://www.comsol.com/showroom/documentation/model/382/〉 (accessed 01.03.12).
[18] Walter H. Gitzen, Alumina as a Ceramic Material, American Ceramic Society, Columbus, OH, 1970.